

ARTICLE OPEN

Unveiling giant hidden Rashba effects in two-dimensional Si₂Bi₂Seungjun Lee¹ and Young-Kyun Kwon¹✉

Recently, it has been known that the hidden Rashba (R-2) effect in two-dimensional materials gives rise to a physical phenomenon called spin-layer locking (SLL). However, not only its underlying fundamental mechanism has been unclear, but also there are only a few materials exhibiting weak SLL. Here, through the first-principles density functional theory and model Hamiltonian calculation, we reveal that the R-2 SLL can be determined by the competition between the sublayer–sublayer interaction and the spin–orbit coupling, which is related to the Rashba strength. In addition, the orbital angular momentum distribution is another crucial point to realize the strong R-2 SLL. We propose that a 2D material Si₂Bi₂ possesses an ideal condition for the strong R-2 SLL, whose Rashba strength is evaluated to be 2.16 eVÅ, which is the greatest value ever observed in 2D R-2 materials to the best of our knowledge. Furthermore, we reveal that the interlayer interaction in a bilayer structure ensures R-2 states spatially farther apart, implying a potential application in spintronics.

npj 2D Materials and Applications (2020)4:45; <https://doi.org/10.1038/s41699-020-00180-2>

INTRODUCTION

The spin–orbit coupling (SOC) combined with an asymmetric crystal potential at surfaces or interfaces induces spin-polarized electronic states, called as Rashba (R-1) spin splitting^{1–3}. The Rashba states exhibit unique band dispersion with spin-momentum locking, which can be described by

$$H_R = -a_R \boldsymbol{\sigma} \times \mathbf{k} \cdot \hat{z}, \quad (1)$$

where a_R , $\boldsymbol{\sigma}$, and \mathbf{k} represent Rashba strength coefficient, Pauli spin matrix vector, and crystal momentum, respectively; and \hat{z} indicates a direction of the local electric field induced by the asymmetric crystal potential. The unique physical properties of the Rashba states have been utilized to realize some crucial concepts in the spintronics^{4,5}, such as spin field transistor^{6,7} and intrinsic spin Hall effects⁸.

It has, however, been reported that the Rashba spin splitting is strongly affected by local orbital angular momentum (OAM) \mathbf{L} in a system with a SOC^{9–12}, which can be described by the orbital Rashba Hamiltonian

$$H_L = -\mathbf{p} \cdot \mathbf{E} = -\gamma \mathbf{k} \times \mathbf{E} \cdot \mathbf{L}, \quad (2)$$

where $\mathbf{p} = \gamma \mathbf{L} \times \mathbf{k}$ is electric dipole moment produced by the asymmetric charge distribution⁹ and γ is a proportional coefficient. Since the Rashba effects from these two model Hamiltonian Eqs. (1) and (2) may not be distinguished in band calculations, Eq. (1) may be used to extract the Rashba strength a_R from the Rashba states.

Since the centrosymmetry guarantees the spin-degenerate electronic structures, only non-centrosymmetric systems have been considered as candidates for the R-1 based spintronics applications. Recently, however, an insight suggested that local symmetry breaking may induce local Rashba (R-2) spin splitting even in centrosymmetric materials^{13,14}. In such systems, intriguingly, degenerate spin states protected by the centrosymmetry are spatially separated into each inversion partner, which can be experimentally detected by spin- and angle-resolved photoemission spectroscopy in both bulk and two-dimensional (2D)

materials^{14–18}. Among materials exhibiting the R-2 effects, bulk systems are not suitable for utilizing the spatially separated states because their localized spin states would be canceled out by their adjacent inversion partners. In the van der Waals (vdW) 2D materials, on the other hand, opposite spins in the degenerate states can be split into top and bottom layers or atomic sublayers (SLs). Such a spatially separated spin splitting is called spin-layer locking (SLL)^{14–16}.

Even though a few experimental observations have shown clear evidences for the existence of the R-2 effects, the following important questions still remain unanswered: (1) Why do some R-2 materials exhibit parabolic band structure rather than the Rashba-like dispersion? (2) How can the R-2 SLL effect be distinguished from unavoidable substrate effects in the experiments¹⁹? (3) Why does the degree of spin segregation depend on the band index of an R-2 material? In addition, some of R-2 materials display an energy gap between the upper and lower R-2 bands, which cannot be described by the conventional Rashba model Hamiltonian given by Eq. (1). Therefore, a model Hamiltonian is required to correctly describe the R-2 SLL. Furthermore, to utilize the R-2 Rashba states in the spintronics applications, it is essentially demanded not only to understand the fundamental physics of the R-2 effects but also to search for 2D materials exhibiting strong R-2 SLL.

To answer and resolve these questions and issues, in this paper, we propose a vdW 2D material Si₂Bi₂ with strong R-2 SLL and explore the physical origins combining the first-principles density functional theory and a model Hamiltonian. We found that the strong SOC restricts wavefunction overlap between local inversion partners and enables the OAM to contribute to the band-selected Rashba effects, leading to the giant R-2 SLL. The Rashba strength of Si₂Bi₂ was calculated to be 2.16 eVÅ, which is the greatest value ever observed in 2D R-2 materials to the best of our knowledge. In addition, we suggest that multilayer configuration may enhance the spatial segregation of spin splitting occurring only at the outermost surfaces, while diminishing almost completely at the inner ones due to the interlayer interactions. Such a stacking

¹Department of Physics and Research Institute for Basic Sciences, Kyung Hee University, Seoul 02447, South Korea. ✉email: ykkwon@khu.ac.kr

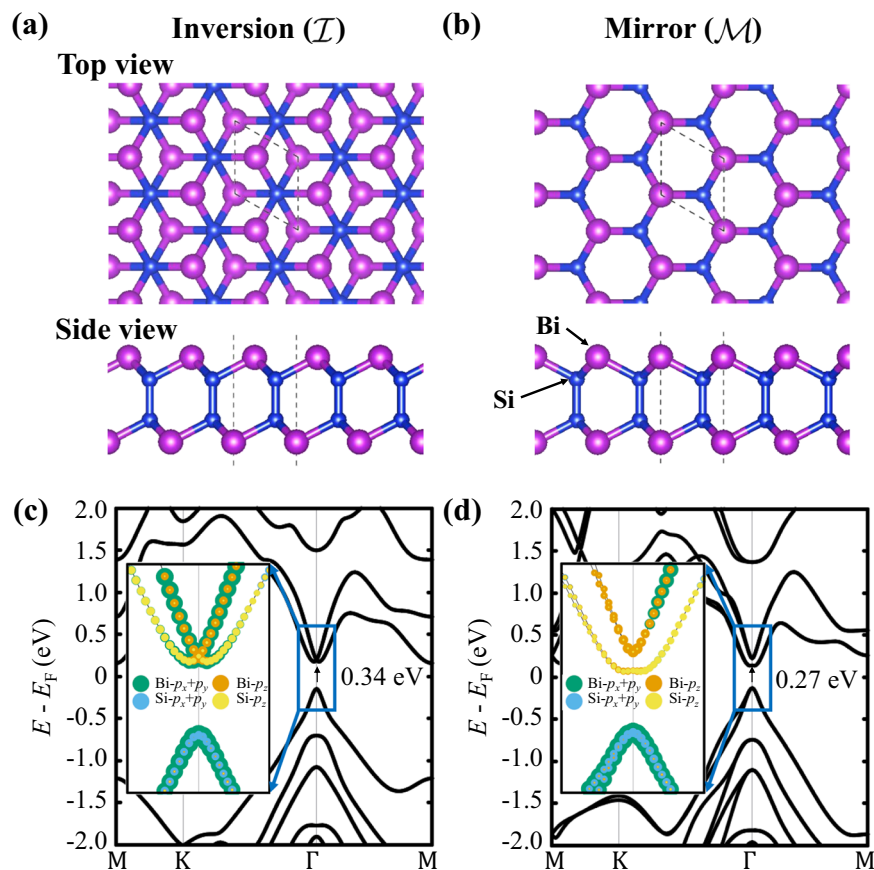


Fig. 1 Crystal and electronic structures of \mathcal{I} and \mathcal{M} - Si_2Bi_2 . Top and side views of the equilibrium crystal structures of Si_2Bi_2 , where Si and Bi atoms are depicted by yellow and purple balls for two different phases with: **a** inversion (\mathcal{I}) and **b** mirror (\mathcal{M}) symmetries, and **c**, **d** their respective electronic band structures, of which the orbital-resolved conduction and valence bands near the Γ point are shown in insets, where each color is assigned to each projected orbital and the line thickness indicates the degree of the orbital contribution. The calculated band gap values at the Γ point are 0.27 and 0.34 eV, respectively.

process eventually leads to the evolution from R-2 to R-1 spin splitting.

RESULTS AND DISCUSSION

Crystal and electronic structures

Earlier studies reported that a group IV element, X ($X = \text{C}, \text{Si}, \text{Ge}, \text{Sn}, \text{or Pb}$) can combine with a group V element, Y ($Y = \text{N}, \text{P}, \text{As}, \text{Sb}, \text{or Bi}$) to form a stable layered compound X_2Y_2 ^{20–22}. Each layered compound can be classified into two groups by the crystal symmetries, one with the \mathcal{I} nversion symmetry ($p\bar{3}m1$) and the other the \mathcal{M} irror one ($p\bar{6}m2$), as shown in Fig. 1a, b. It is noted that the space groups of these two crystal phases of X_2Y_2 are essentially the same as those of the 1H and 1T phases of transition metal (M) dichalcogenides (A_2), MA_2 , with the correspondences of X_2 and Y to M and A, respectively. Among various group IV–V compounds, we propose that Si_2Bi_2 becomes an exemplary material exhibiting strong R-2 type Rashba effects. It was found that both \mathcal{I} and \mathcal{M} phases of Si_2Bi_2 are stable with their energy difference of <3 meV per atom²².

Fig. 1c, d show their corresponding electronic band structures calculated using the PBE XC functional, and their orbital-resolved ones in the respective insets, which will be discussed later. Both \mathcal{I} - and \mathcal{M} -phases have a band gap of 0.34 and 0.27 eV at the Γ point. It is noted that the \mathcal{I} -phase is an indirect band gap semiconductor with 0.31 eV since the conduction band at the M point is slightly

lower than that at the Γ point. The inversion symmetry in the \mathcal{I} phase guarantees degenerate spin states, whereas the mirror symmetry in the \mathcal{M} phase lifts the degeneracy. Nevertheless, both phases revealed the Rashba-type splitting near their conduction band minima, but not near the valence band maxima in their band structures. To verify that such a Rashba-type splitting is not a functional-dependent artifact, we also used the HSE06 XC functional, which yields Rashba-like band structures in both phases as shown in Supplementary Fig. 1. To get a better understanding of these unusual Rashba effects, we first focus our discussion on the \mathcal{I} phase with higher symmetric features and then on the \mathcal{M} phase.

Hidden Rashba spin-layer locking

To verify if the Bi–Si system indeed produces the Rashba splitting, as a first step, we constructed an artificial substructure composed of Bi–Si monolayer with a broken inversion symmetry as shown in Fig. 2a. The dangling bond of each Si atom in the 2D SiBi monolayer was saturated by a hydrogen atom. Due to the atomic arrangement of Bi–Si and the difference in their electron affinities, its strong asymmetric local potential shown in Fig. 2a induces an electric field perpendicular to its plane. We calculated its electronic band structure shown in Supplementary Fig. 2. In the absence of SOC, as shown in Fig. 2b, the lowest conduction band (CB1) exhibits spin-degenerate parabolic dispersion relation and is mainly formed by the Bi p_z orbital. With SOC turned-on, the

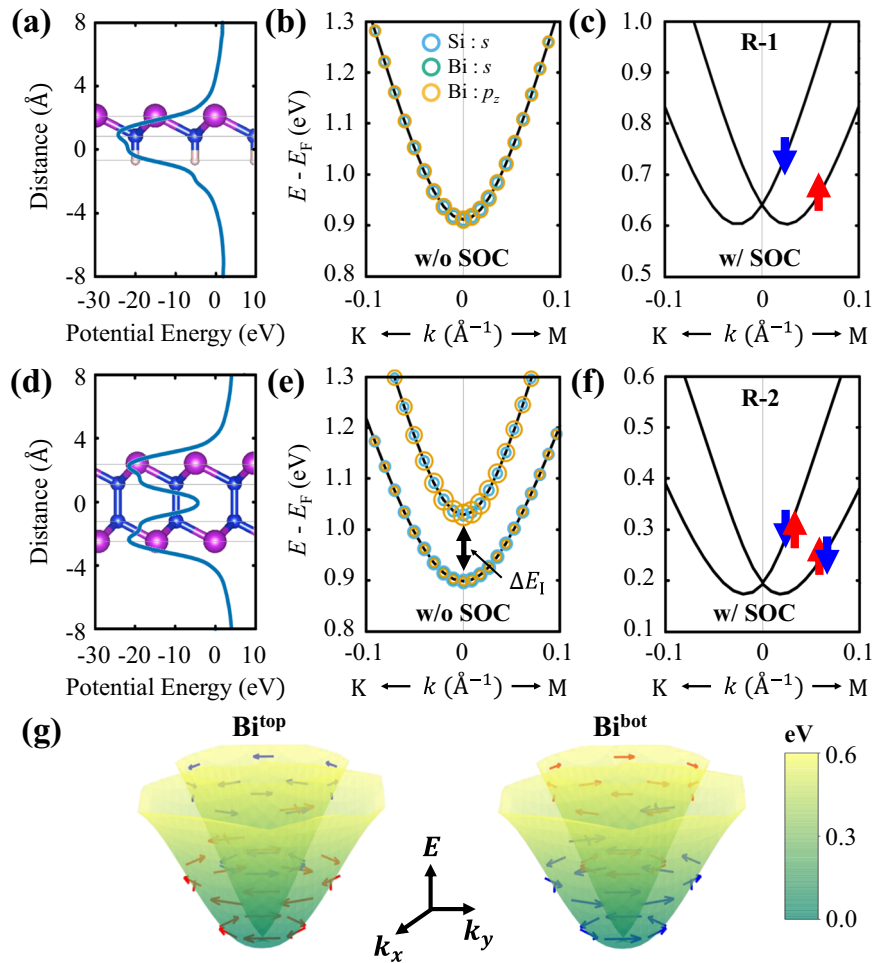


Fig. 2 Hidden Rashba spin-layer locking in $I\text{-Si}_2\text{Bi}_2$. Plane-averaged electrostatic potentials and electronic structures near the conduction band minima of an artificially constructed asymmetric 2D SiBi monolayer (a–c) and $I\text{-Si}_2\text{Bi}_2$ (d–f). The respective structures, in which Si and Bi atoms are depicted by the purple and blue spheres, respectively, are overlaid in (a) and (d). The dangling bond of each Si atom in (a) is saturated with a hydrogen atom depicted with the white sphere. The electronic band structures are shown without SOC in (b) and (e), and with SOC in (c) and (f). The latter two cases clearly show the Rashba band splittings, one with the R-1 and the other with the R-2. Local orbital contributions are displayed with skyblue, green, and yellow circles for Si s , Bi s , and p_z orbitals, respectively. The radius of circle indicates the degree of the orbital contribution. The ΔE_1 in (e) indicates the splitting energy between CB1 and CB2 due to the interaction between the top and bottom SLs. The red and blue arrows denote spin states in (c) and (f). (g) Spin textures spatially resolved on the top (left) and bottom (right) Bi SLs, or Bi^{top} and Bi^{bot} , plotted on the Rashba bands shown in (f). Red (blue) arrows represent the clockwise (counterclockwise) spin chirality and the colorbox indicates energy scale in eV relative to the bottom of the conduction band.

p_z orbital related to the in-plane OAM can give a significant contribution to the Rashba interaction due to the out-of-plane local electric field, as described in Eq. (2). Thus, the 2D SiBi monolayer exhibits a typical R-1 spin splitting as shown in Fig. 2c.

In the real $I\text{-Si}_2\text{Bi}_2$ material, however, the underlying physics becomes much more complicated because SL–SL interaction also takes part in determining its electronic structure. Similar to Fig. 2a, we also computed the local electrostatic potential of $I\text{-Si}_2\text{Bi}_2$ displayed in Fig. 2d. Due to the inversion symmetry, there is no net dipole moment. However, the potential profile clearly indicates that there are local dipole moments on the top and bottom SLs, which are oppositely oriented to each other. Were it not for both SL–SL interaction and SOC, $I\text{-Si}_2\text{Bi}_2$ should have had the four-fold degenerate conduction bands composed mainly of the p_z orbitals with spin-up and -down of the top and bottom Bi SLs. Now, only turning on SOC, the opposite local electric fields, each on each SL, should have induced the spatially separated R-2 spin splitting, but the inversion symmetry still guarantees the spin degeneracy, which are schematically summarized in Supplementary Fig. 3.

There is, however, an inevitable interaction between the top and bottom SLs, which lifts their four-fold degeneracy via the wavefunction overlap even without SOC, as shown in Fig. 2e. The splitting energy ΔE_1 due to such interaction was calculated to be 0.13 eV at the Γ point. One could expect that SOC would split these bands further into two sets of Rashba bands, which is, however, contradictory to degeneracy guaranteed by the inversion symmetry. It was, instead, surprisingly found that turning on SOC converted two separated doubly degenerate parabolic bands (Fig. 2e) to almost perfect and doubly degenerate Rashba bands, as shown in Fig. 2f, essentially the same as those expected in the case without the SL–SL interaction as described above, and in Supplementary Fig. 3.

To confirm that such bands are the hidden Rashba bands, we explored the doubly degenerate Rashba bands (Fig. 2f) by computing the spatially resolved spin textures on the top (Bitop) and bottom (Bibot) Bi atom SLs, shown in Fig. 2g. For a given (n, \mathbf{k}) , the spin polarization is the expectation value of the spin operator, that is, $\boldsymbol{\mu}_{n,\mathbf{k}} \propto \langle \psi_{n,\mathbf{k}} | \boldsymbol{\sigma} | \psi_{n,\mathbf{k}} \rangle$, where $\boldsymbol{\sigma}$ is the Pauli spin matrix vector. Its projection on each atom a , $\boldsymbol{\mu}_{n,\mathbf{k}}^a$, was obtained by expanding $\boldsymbol{\mu}_{n,\mathbf{k}}$ in terms of the spherical harmonics $|Y_m^a\rangle$ with the

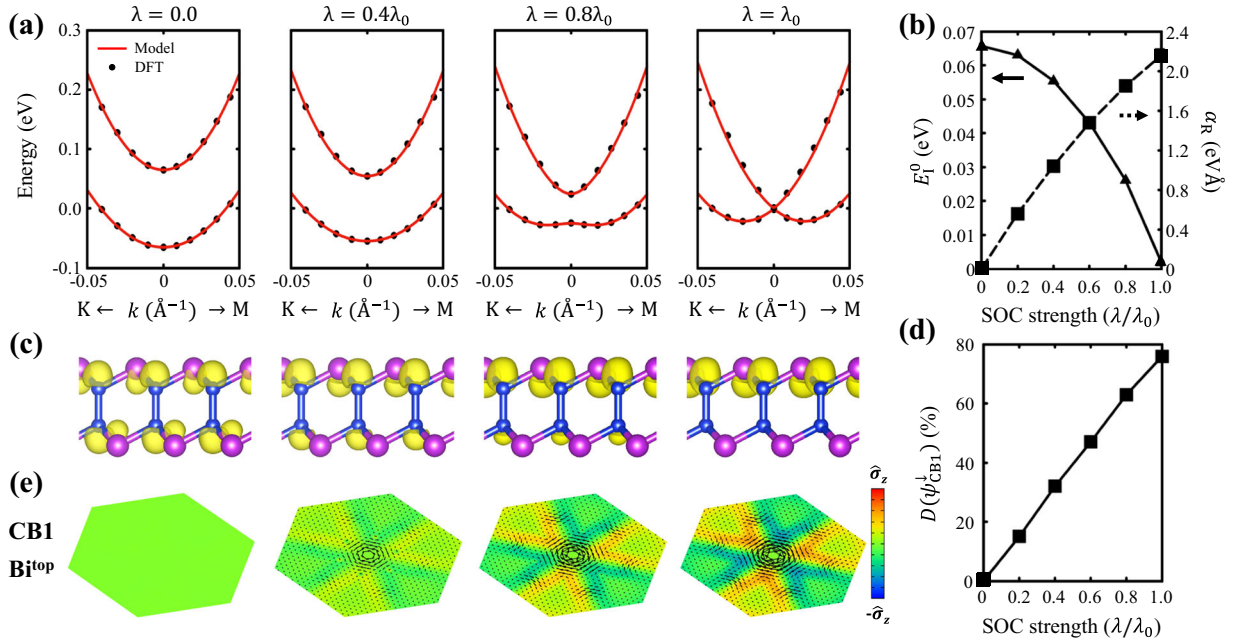


Fig. 3 Role of the spin-orbit coupling in the spin-layer locking. Evolution of the electronic structure with the SOC strength $\lambda/\lambda_0 \in (0, 1)$, where λ_0 is the real SOC strength: **a** two lowest conduction bands near the Γ point. The black dots show the energy eigenvalues calculated by DFT, which were fitted by the model defined in Eq. (3), plotted with red solid lines. **b** λ -dependence of the interaction energy (E_1^0) and the Rashba strength (α_R) fitted in (a). **c** $|\psi_{CB1}^\perp|^2$, spin-resolved wavefunction squared, calculated at $\mathbf{k}_{\Gamma-M} = (0.015, 0)(2\pi/a)$ near the Γ point. **d** Degree of wavefunction segregation $D(\psi)$ defined in Eq. (5) evaluated from (c) as a function of λ . **e** Spatially resolved spin maps on the top Bi atom layer plotted in the first Brillouin zone for the lowest conduction band. The size of black arrows and different colors indicate the in-plane and out-of-plane spin components.

orbital angular momentum (l, m) of the a atom, or $\mu_{n,\mathbf{k}}^a \propto \sum_{l,m} \langle \psi_{n,\mathbf{k}} | \sigma | Y_{lm}^a \rangle \langle Y_{lm}^a | \psi_{n,\mathbf{k}} \rangle$. The spin map on each layer exhibits the opposite spin chiralities on the inner and outer Rashba bands, as usually observed in non-centrosymmetric systems. Even more intriguingly, these spin chiralities are spatially coupled to the layers. The spins of Bi^{top} on the inner band rotate in one way (e.g., counterclockwise, blue arrows in the left image), whereas those of Bi^{bot} do in the other way (clockwise, red arrows on the right image). On the outer band, their corresponding spins rotate the other way around (red arrows on the left and blue arrows on the right images). This observation clearly reveals the strong R-2 SLL phenomenon. Furthermore, it is worthwhile to note the relation between the local symmetry breaking and the orbital polarization described in Eq. (2). We investigated the OAM distributions²³ of both the 2D SiBi monolayer and \mathcal{I} -Si₂Bi₂ as described in Methods section, and found that the \mathcal{I} -Si₂Bi₂ exhibits the hidden orbital polarization as well as the R-2 SLL induced by the local symmetry breaking. For detailed description, see Supplementary Note 1 with Supplementary Figs. 4 and 5.

In view of previous results observed in other 2D R-2 materials, such as PtSe₂¹⁶ or bilayer WSe₂¹⁴, which have revealed the SLL phenomena, but still with parabolic bands similar to those shown in Fig. 2e, our hidden Rashba bands shown in Fig. 2f are exceptionally unusual since they look like the Rashba-like bands shown in Fig. 2c. To answer what causes such distinction, we examined the pathway from the parabolic bands (Fig. 2e) to the Rashba-like ones (Fig. 2f), while manipulating the SOC strength $\lambda/\lambda_0 \in (0, 1)$, where λ_0 is the real SOC strength of our \mathcal{I} -Bi₂Si₂ system. As λ increases, two split bands tend to form a Rashba-like bands through continuous change as shown in Fig. 3a. This result indicates that the competition between the SL–SL interaction (ΔE_1) and the Rashba strength (α_R) determines the shape of electronic bands.

To understand such competition quantitatively, we devised a simplest model Hamiltonian represented by four minimal basis vectors that describes SL–SL interaction and Rashba splitting. For more detailed description of our model Hamiltonian, see Supplementary Note 2. From the model Hamiltonian, we obtained two doubly degenerate bands

$$E_{\pm} = \frac{\hbar^2 k^2}{2m^*} \pm \sqrt{(\alpha_R k)^2 + (E_1^0 + E_1^1 k^2)^2}, \quad (3)$$

guaranteed by inversion symmetry. Here m^* is the effective mass, E_1^0 and E_1^1 are the SL–SL interaction coefficients. To discover how to compete the SL–SL interaction with Rashba spin splitting, the DFT bands (black dots) were fitted to the model bands (red lines) given in Eq. (3), resulting in almost perfect agreement as shown in Fig. 3a. The fitted parameters E_1^0 and α_R as a function of λ are shown in Fig. 3b. As expected, SOC weakens the SL–SL interaction, but strengthens α_R , which was calculated to be 2.16 eVÅ at $\lambda = \lambda_0$. This value is much larger than those observed in metal surfaces, for example, Au(111) (0.33 eVÅ)²⁴, Bi(111) (0.55 eVÅ)²⁵, as well as other materials exhibiting the R-2 SOC such as BaNiS₂ (0.24 eVÅ)²⁶, and is also comparable with conventional giant Rashba system, such as hybrid perovskites (1.6 eVÅ)²⁷, BiSb monolayer (2.3 eVÅ)²⁸, or BiTeI (3.8 eVÅ)²⁹. Therefore, we may classify our system into the giant hidden Rashba material.

This result was further confirmed by $|\psi_{CB1}^\perp(r)|^2$, obtained from the spin-resolved wavefunction yielded near the Γ point. As shown in Fig. 3c, it evolves from an even distribution on both SLs at $\lambda = 0$ toward a complete spatial segregation at $\lambda = \lambda_0$, which is quantified by $D(\psi)$, defined by Eq. (5), shown in Fig. 3d. For every λ value, we also reckoned the spatially resolved spin map on the Bi^{top} SL to verify the degree of the SLL, which is shown in Fig. 3e. We emphasize that no sharp phase transition was observed and thus even for $\lambda < \lambda_0$, the system exhibits the SLL while maintaining

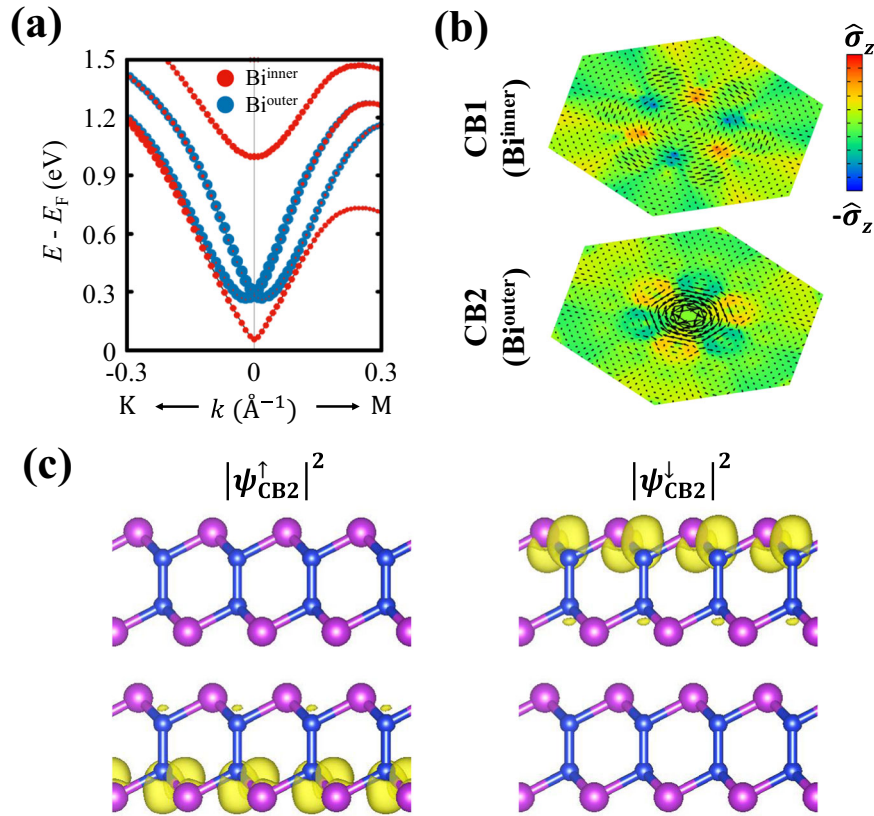


Fig. 4 Effect of the interlayer interaction on hidden Rashba states. **a** Four lowest conduction bands (CB1 through CB4 in ascending order in energy) of a \mathcal{I} -Si₂Bi₂ bilayer spatially resolved on the inner Bi SLs, Bi^{inner} (red circles) and on the outer ones, Bi^{outer} (blue circles). The size of circles indicates the amount of their contributions, which are well separated especially near the Γ point. **b** Spin textures computed from CB1 and CB2 localized on Bi^{inner} and Bi^{outer}, respectively. The size of black arrows and different colors indicate, respectively, the in-plane and out-of-plane spin components. **c** Spatially projected spinor wavefunction squared, $|\psi_{CB2}^\sigma|^2$, with $\sigma = \uparrow$ and \downarrow for the CB2 band evaluated at $k = 0.03\pi a^{-1}$ along the $\Gamma - M$ line close to the Γ point.

two parabolic bands due to appreciable SL–SL interaction. When λ becomes λ_0 eventually, all three features clearly reveal complete Rashba-like bands, wavefunction segregation, and SLL implying that our system, 2D \mathcal{I} -Si₂Bi₂ possesses vastly strong SOC minimizing the SL–SL interaction. We further notice that when λ becomes larger than λ_0 , energy gap between CB1 and CB2 reopens, while wavefunctions are still strongly segregated and R-2 SLL is also vivid, as shown in Supplementary Fig. 6.

On the other hand, we noticed that there is no Rashba spin splitting at the highest valence band (VB1) unlike at CB1, perusing the band structures shown in Fig. 1c. As shown in the inset of Fig. 1c and Supplementary Fig. 7a, there is nearly no p_z orbital contribution at VB1, resulting in no OAM distribution to produce Rashba spin splitting even with strong SOC, which is clear from Eq. (2). This non-Rashba feature observed in the VB1 was further confirmed by the spin texture and the wavefunction segregation computed on the VB1 shown in Supplementary Fig. 7b,c. Therefore, to utilize an R-2 material in the spintronics application, its hidden Rashba SLL should be induced by the bands near the Fermi level, which possess the OAM perpendicular to the local electric field.

At this time, it is worth mentioning that the spin splitting was also observed in \mathcal{M} -Si₂Bi₂ with the broken inversion symmetry, which additionally lifts the degeneracy protected in the \mathcal{I} -counterpart and guarantees the Dresselhaus spin splitting³⁰. Intriguingly, we also observed a strong SLL in a few lowest conduction bands near the Γ point, as shown in Supplementary Fig. 8. Such strong SLL is also attributed to the OAM similar in its inversion

counterpart. Here, we again emphasize that the OAM is an important factor to determine the SLL.

Effects of the interlayer interaction

Since 2D materials usually form multilayers rather than monolayers, it is also of importance to understand the effect of the interlayer or vdW interaction on the SLL phenomenon. To do this, we constructed a bilayer of \mathcal{I} -Si₂Bi₂ with AA stacking which still maintains the inversion symmetry, and investigated its electronic properties. Figure 4a shows its four lowest conduction bands (CB1 through CB4 in ascending order in energy) represented by the projections on the inner Bi (Bi^{inner}) SLs in red circles and on their outer (Bi^{outer}) counterparts in blue circles. The widely split two red bands (CB1 and CB4) are contributed mostly by the Bi^{inner} SLs, whereas the Rashba-like blue bands (CB2 and CB3) mostly by the Bi^{outer} ones. Were it not for the vdW interaction, two identical monolayers should have shown exactly the same band structures as shown in Fig. 2f, with every band four-fold degenerated. One can, however, easily expect that the Bi^{inner} SLs are directly affected by the vdW interaction, whereas the Bi^{outer} SLs are intact. Thus it can be explained that the vdW interaction caused the band repulsion between CB1 and CB4, while the CB2 and CB3 localized at two opposite Bi^{outer} SLs preserve the SLL induced in each isolated monolayer.

Our explanation becomes even clearer from the spatially resolved spin textures and spinor wavefunctions. Spin texture of the Bi^{outer} SLs evaluated on the CB2 does show much stronger spin chirality implying stronger SLL than that of the Bi^{inner} SLs on the CB1, where R-2 Rashba effects are suppressed, as shown in Fig. 4b. To verify if the

SLL in the bilayer is indeed from CB2 and CB3, we represented the spinor wavefunctions squared, $|\psi_n^\sigma|^2$ in real space. In Fig. 4c, those for $\sigma = \uparrow$ and \downarrow calculated on the $n = \text{CB2}$ clearly display spatially segregated spin states demonstrating the strong SLL. It is worthy of mentioning that each band still doubly degenerates since the bilayer configuration also possesses the inversion symmetry. In other words, it is the interlayer interaction that removes the R-2 effect at the inner surfaces, but the Rashba states survive only at the outer surfaces of the bilayer. This spatial segregation would be utilized in some spintronics applications since one could control the spin behaviors only on the top surface without being influenced by those on the bottom one. We also noticed that when the layered R-2 materials become a bulk structure, Rashba spin splittings inside bulk region may be removed as seen in the bilayer, and only the surface Rashba states survive, implying that the R-2 SLL automatically changes to the R-1 spin splitting. It is, therefore, the local symmetry breaking that is the physical origin causing not only the R-2 SLL, but also R-1 effects.

In summary, using first-principles density functional theory, we predicted a 2D material, which is layered Si_2Bi_2 exhibiting the giant R-2 SLL. To understand an underlying physical origin of the R-2 SLL, we performed first-principles calculations as well as solved a devised model Hamiltonian to describe the R-2 SLL. Through this model calculation, we found that there is a competition between SOC and SL–SL interaction to reveal the R-2 SLL. As the former, as it increases, weakens the latter and strengthens α_R , it is leading to the giant hidden Rashba spin splitting. Furthermore, we found that the R-2 SLL is also closely related to the OAM distribution. The Rashba strength in Si_2Bi_2 was calculated to be $2.16 \text{ eV}\text{\AA}$, which is the greatest value ever observed in R-2 materials to the best of our knowledge. We also revealed from a bilayer case that the R-2 SLL can be removed at the inner surfaces due to the interlayer interaction, but remained spatially farther apart at the outer surfaces. This eventually leads to a conclusion that the R-1 effect is also originated from the same local symmetry breaking causing the R-2 SLL. Our findings may not only uncover the fundamental physics of R-2 SLL, but also provide a guidance for searching R-2 materials.

METHODS

Density functional calculation

To understand the underlying physics of the R-2 SLL in 2D Si_2Bi_2 , we performed first-principles calculations based on density functional theory³¹ as implemented in Vienna ab initio simulation package (VASP)³². The electronic wavefunctions were expanded by plane wave basis with kinetic energy cutoff of 500 eV. We employed the projector-augmented wave pseudopotentials^{33,34} to describe the valence electrons, and treated exchange-correlation (XC) functional within the generalized gradient approximation of Perdew-Burke-Ernzerhof (PBE)³⁵ with non-collinear spin polarization³⁶. To rule out any functional-related artifacts, we verified our PBE-based results using hybrid functional (HSE06)³⁷. For bilayer calculations, in which interlayer interaction cannot be neglected, Grimme-D2 Van der Waals correction³⁸ was added. To mimic 2D layered structure in periodic cells, we included a sufficiently large vacuum region in-between neighboring cells along the out-of-plane direction. The Brillouin zone (BZ) of each structure was sampled using a $30 \times 30 \times 1$ k -point mesh according to the Monkhost-Pack scheme³⁹.

Manipulation of spin-orbit interaction

To describe and visualize the R-2 SLL, we included spin-orbit interaction in the all calculation. The SOC is described by an additional Hamiltonian

$$H_{\text{SOC}}^{\alpha\beta} = \frac{\hbar^2}{(2m_e c)^2} \frac{K(r)}{r} \frac{dV(r)}{dr} \boldsymbol{\sigma}^{\alpha\beta} \cdot \mathbf{L}, \quad (4)$$

where α and β indicate spin-up and -down components of the spinor wave function, $\boldsymbol{\sigma}$ and \mathbf{L} are Pauli spin matrices and angular momentum operator, $V(r)$ is the spherical part of the effective all electron potential within the

PAW sphere, and

$$K(r) = \left(1 - \frac{V(r)}{(2m_e c)^2} \right)^{-2},$$

as explained earlier^{36,40}. To explore the effect of the SOC strength, we introduced an artificial parameter λ which scales Eq. (4) as

$$H_{\text{SOC}}^{\alpha\beta}(\lambda) = \frac{\lambda}{\lambda_0} H_{\text{SOC}}^{\alpha\beta}.$$

When $\lambda = \lambda_0$, it becomes the full SOC Hamiltonian given in Eq. (4).

Visualization of spin-layer locking

The momentum-resolved spinor wavefunctions were evaluated by projecting the two-component spinor

$$|\psi_{n\mathbf{k}}\rangle = \begin{pmatrix} \psi_{n\mathbf{k}}^\uparrow \\ \psi_{n\mathbf{k}}^\downarrow \end{pmatrix}$$

into spherical harmonics Y_{lm}^a centered at ion index a with angular momentum quantum numbers (l, m) . Here, n and \mathbf{k} are band index and crystal momentum, and the arrows \uparrow and \downarrow represent spin-up and -down. Such projected components were further manipulated to understand the contribution of each orbital angular momentum to the band structures and to generate the atom-resolved spin texture map.

To verify the SLL in our system, we quantify the spatial spin separation by introducing the degree of wavefunction segregation (DWS) $D(\psi_{n\mathbf{k}}^\sigma)$ defined as²⁶

$$D(\psi_{n\mathbf{k}}^\sigma) = \frac{|P_{\psi_{n\mathbf{k}}}^\sigma(S_\alpha) - P_{\psi_{n\mathbf{k}}}^\sigma(S_\beta)|}{|P_{\psi_{n\mathbf{k}}}^\sigma(S_\alpha) + P_{\psi_{n\mathbf{k}}}^\sigma(S_\beta)|}, \quad (5)$$

with

$$P_{\psi_{n\mathbf{k}}}^\sigma(S_i) = \int_{\Omega \in S_i} |\psi_{n\mathbf{k}}^\sigma(\mathbf{r})|^2 d^3\mathbf{r}, \quad (6)$$

where $\sigma = \uparrow$ and \downarrow , n is band index, and S_i indicates the real space sector for the upper Bi–Si ($i = \alpha$) or lower Si–Bi ($i = \beta$) SL. $P_{\psi_{n\mathbf{k}}}^\sigma(S_\alpha)$, for example, represents the wavefunction $\psi_{n,\mathbf{k}}^\sigma$ localized on the upper SL sector S_α .

DATA AVAILABILITY

The data generated and/or analysed during the current study are available from the corresponding author on reasonable request.

Received: 24 July 2020; Accepted: 12 November 2020;

Published online: 11 December 2020

REFERENCES

- Rashba, E. I. Properties of semiconductors with an extremum loop. 1. Cyclotron and combinational resonance in a magnetic field perpendicular to the plane of the loop. *Sov. Phys. Solid State* **2**, 1109–1122 (1960).
- Bychkov, Y. A. & Rashba, E. I. Properties of a 2d electron gas with lifted spectral degeneracy. *JETP Lett.* **39**, 78 (1984).
- Manchon, A., Koo, H. C., Nitta, J., Frolov, S. M. & Duine, R. A. New perspectives for Rashba spin-orbit coupling. *Nat. Mater.* **14**, 871–882 (2015).
- Fabian, J., Matos-Abiague, A., Ertler, C., Stano, P. & Zutic, I. Semiconductor spintronics. *Phys. Rev.* **57**, 565–907 (2007).
- Chappert, C., Fert, A. & Van Dau, F. N. The emergence of spin electronics in data storage. *Nat. Mater.* **6**, 813–823 (2007).
- Datta, S. & Das, B. Electronic analog of the electro-optic modulator. *Appl. Phys. Lett.* **56**, 665 (1990).
- Koo, H. C. et al. Control of spin precession in a spin-injected field effect transistor. *Science* **325**, 1515–1518 (2009).
- Sinova, J. et al. Universal intrinsic spin hall effect. *Phys. Rev. Lett.* **92**, 126603 (2004).
- Park, S. R., Kim, C. H., Yu, J., Han, J. H. & Kim, C. Orbital-angular-momentum based origin of Rashba-type surface band splitting. *Phys. Rev. Lett.* **107**, 156803 (2011).
- Park, J.-H., Kim, C. H., Rhim, J.-W. & Han, J. H. Orbital Rashba effect and its detection by circular dichroism angle-resolved photoemission spectroscopy. *Phys. Rev. B* **85**, 195401 (2012).
- Kim, B. et al. Spin and orbital angular momentum structure of cu(111) and au(111) surface states. *Phys. Rev. B* **85**, 195402 (2012).

12. Kim, B. et al. Microscopic mechanism for asymmetric charge distribution in Rashba-type surface states and the origin of the energy splitting scale. *Phys. Rev. B* **88**, 205408 (2013).
13. Zhang, X., Liu, Q., Luo, J.-W., Freeman, A. J. & Zunger, A. Hidden spin polarization in inversion-symmetric bulk crystals. *Nat. Phys.* **10**, 387–393 (2014).
14. Riley, J. M. et al. Direct observation of spin-polarized bulk bands in an inversion-symmetric semiconductor. *Nat. Phys.* **10**, 835–839 (2014).
15. Razzoli, E. et al. Selective probing of hidden spin-polarized states in inversion-symmetric bulk MoS_2 . *Phys. Rev. Lett.* **118**, 086402 (2017).
16. Yao, W. et al. Direct observation of spin-layer locking by local Rashba effect in monolayer semiconducting PtSe_2 film. *Nat. Commun.* **8**, 14216 (2017).
17. Santos-Cottin, D. et al. Rashba coupling amplification by a staggered crystal field. *Nat. Commun.* **7**, 11258 (2016).
18. Wu, S.-L. et al. Direct evidence of hidden local spin polarization in a centrosymmetric superconductor $\text{LaO}_{0.55}\text{F}_{0.45}\text{BiS}_2$. *Nat. Commun.* **8**, 1919 (2017).
19. Li, P. & Appelbaum, I. Illuminating “spin-polarized” Bloch wave-function projection from degenerate bands in decomposable centrosymmetric lattices. *Phys. Rev. B* **97**, 125434 (2018).
20. Özdamar, B. et al. Structural, vibrational, and electronic properties of single-layer hexagonal crystals of group IV and V elements. *Phys. Rev. B* **98**, 045431 (2018).
21. Zhang, W., Yin, J., Ding, Y., Jiang, Y. & Zhang, P. Strain-engineering tunable electron mobility of monolayer IV-V group compounds. *Nanoscale* **10**, 16750–16758 (2018).
22. Lee, S. & Kwon, Y.-K. Versatile physical properties of a novel two-dimensional materials composed of group IV-V elements. Preprint at <https://arXiv.org/abs/2007.05137> (2020).
23. Ryoo, J. & Park, C. Hidden orbital polarization in diamond, silicon, germanium, gallium arsenide and layered materials. *NPG Asia Mater.* **9**, e382 (2017).
24. LaShell, S., McDougall, B. A. & Jensen, E. Spin splitting of an $\text{Au}(111)$ surface state band observed with angle resolved photoelectron spectroscopy. *Phys. Rev. Lett.* **77**, 3419–3422 (1996).
25. Koroteev, Y. M. et al. Strong spin-orbit splitting on Bi surfaces. *Phys. Rev. Lett.* **93**, 046403 (2004).
26. Yuan, L. et al. Uncovering and tailoring hidden Rashba spin-orbit splitting in centrosymmetric crystals. *Nat. Commun.* **10**, 906 (2019).
27. Zhai, Y. et al. Giant Rashba splitting in 2d organic-inorganic halide perovskites measured by transient spectroscopies. *Sci. Adv.* **3**, e1700704 (2017).
28. Singh, S. & Romero, A. H. Giant tunable Rashba spin splitting in a two-dimensional BiSb monolayer and in BiSb/AlN heterostructures. *Phys. Rev. B* **95**, 165444 (2017).
29. Ishizaka, K. et al. Giant Rashba-type spin splitting in bulk BiTeI. *Nat. Mater.* **10**, 521–526 (2011).
30. Dresselhaus, G. Spin-orbit coupling effects in zinc blende structures. *Phys. Rev.* **100**, 580–586 (1955).
31. Kohn, W. & Sham, L. J. Self-consistent equations including exchange and correlation effects. *Phys. Rev.* **140**, A1133–A1138 (1965).
32. Kresse, G. & Furthmüller, J. Efficient iterative schemes for ab initio total-energy calculations using a plane-wave basis set. *Phys. Rev. B* **54**, 11169–11186 (1996).
33. Blöchl, P. E. Projector augmented-wave method. *Phys. Rev. B* **50**, 17953–17979 (1994).
34. Kresse, G. & Joubert, D. From ultrasoft pseudopotentials to the projector augmented-wave method. *Phys. Rev. B* **59**, 1758–1775 (1999).
35. Perdew, J. P., Burke, K. & Ernzerhof, M. Generalized gradient approximation made simple. *Phys. Rev. Lett.* **77**, 3865–3868 (1996).
36. Steiner, S., Khmelevskiy, S., Marsmann, M. & Kresse, G. Calculation of the magnetic anisotropy with projected-augmented-wave methodology and the case study of disordered $\text{Fe}_{1-x}\text{Co}_x$ alloys. *Phys. Rev. B* **93**, 224425 (2016).
37. Krukau, A. V., Vydrov, O. A., Izmaylov, A. F. & Scuseria, G. E. Influence of the exchange screening parameter on the performance of screened hybrid functionals. *J. Chem. Phys.* **125**, 224106 (2006).
38. Grimme, S. Semiempirical GGA-type density functional constructed with a long-range dispersion correction. *J. Comput. Chem.* **27**, 1787–1799 (2006).
39. Monkhorst, H. J. & Pack, J. D. Special points for Brillouin-zone integrations. *Phys. Rev. B* **13**, 5188 (1976).
40. Lenthe, E.V., Baerends, E. J. & Snijders, J. G. Relativistic regular two-component hamiltonians. *J. Chem. Phys.* **99**, 4597–4610 (1993).

ACKNOWLEDGEMENTS

We gratefully acknowledge financial support from the South Korean government through the National Research Foundation (NRF) of Korea (No. 2019R1A2C1005417). Some portion of our computational work was done using the resources of the KISTI Supercomputing Center (KSC-2018-CHA-0052 and KSC-2020-CRE-0011).

AUTHOR CONTRIBUTIONS

S.L. performed all the calculations and analyzed the data with help from Y.-K.K., S.L. and Y.-K.K. wrote the manuscript. Y.-K.K. supervised the whole project.

COMPETING INTERESTS

The authors declare no competing interests.

ADDITIONAL INFORMATION

Supplementary information is available for this paper at <https://doi.org/10.1038/s41699-020-00180-2>.

Correspondence and requests for materials should be addressed to Y.-K.K.

Reprints and permission information is available at <http://www.nature.com/reprints>

Publisher's note Springer Nature remains neutral with regard to jurisdictional claims in published maps and institutional affiliations.



Open Access This article is licensed under a Creative Commons Attribution 4.0 International License, which permits use, sharing, adaptation, distribution and reproduction in any medium or format, as long as you give appropriate credit to the original author(s) and the source, provide a link to the Creative Commons license, and indicate if changes were made. The images or other third party material in this article are included in the article's Creative Commons license, unless indicated otherwise in a credit line to the material. If material is not included in the article's Creative Commons license and your intended use is not permitted by statutory regulation or exceeds the permitted use, you will need to obtain permission directly from the copyright holder. To view a copy of this license, visit <http://creativecommons.org/licenses/by/4.0/>.

© The Author(s) 2020